MODELING AERODYNAMICS FOR COMPREHENSIVE ANALYSIS OF HELICOPTER ROTORS

Khiem-Van Truong
truong@onera.fr
ONERA, The French Aerospace Lab
Châtillon, France

ABSTRACT

To fulfill the objective of design tools, comprehensive analysis codes need to be capable of providing both accurate and time-efficient predictions of rotor airloads. The coupling of high-fidelity computational fluid dynamics CFD with comprehensive analysis codes has showed improved predictions of airloads, but such approach is very expensive in terms of CPU time and cannot be used for design. The aerodynamics environment about helicopter rotors is very complex, encompassing subsonic to transonic flow with unsteady, stalled regimes and 3-D effects. Semi-empirical models of dynamic stall were created for modeling unsteady aerodynamics including stalled flow. Most of them, developed from the 1970s through the 1990s, were found unsuccessful to reproduce experimental results on the UH-60A helicopter. Most dynamic stall models also suffered problems of numerical convergence. Thus, there are two levels of difficulties for semi-empirical models: providing good physics description of aerodynamics and ensuring numerical convergence when implemented in comprehensive analysis codes. The present communication is concerned about the revision of the "ONERA Hopf Bifurcation model". The model takes into account various aerodynamic phenomena, unsteady behavior before stall onset, stall delay, vortex-shedding phenomenon and boundary-layer effects that have been overlooked. 3-D effects are not still well investigated and their complexity is accounted for by sweep effects, rotation effects and transonic tip relief effects. For the extreme aerodynamic condition of high-speed flight, a correction outside of the stall model, is suggested for the induced velocity. The implementation of the model into a comprehensive analysis code ensuring the numerical convergence is presented. The experimental results obtained in the wind tunnel S1 of Modane (France) in 1991 on the rotor 7A are considered for illustration of the capabilities of the stall model. There are three test conditions considered: high-speed test point, high-thrust test point with light stall and high-thrust test point with deep stall. Since tests were made in wind tunnel, corrections for test environment involving wind tunnel walls and the test stand, and for Reynolds effects are necessary. The prediction of the airloads and structural loads of all the test points considered is quite in reasonable agreement with the experimental results and requires very low CPU time demands.

NOTATION

C_i $(i = 1,2,3)$	aerodynamic coefficient (i=1: lift; i=2: pitching moment, i=3: drag)
$C_{1,i}$ $(i = 1,2,3)$	in the regime of attached flow
$C_{2,i}$ $(i = 1,2,3)$	in the regime of separated flow
M	Mach number
R_e	Reynolds number
α	aerodynamic incidence angle
α_{cr}	critical stall angle
r_n	normalized radial distance
R	blade radius
Λ_{deg}	sweep angle, expressed in degrees

1 INTRODUCTION

To fulfill the objective of design tools, comprehensive analysis codes need to be capable of providing both accurate and time-efficient predictions of rotor airloads. The coupling of high-fidelity computational fluid dynamics CFD with comprehensive analysis codes has showed improved predictions of airloads on the UH-60A [22], but such approach is very expensive in terms of CPU time and cannot be used for design. The aerodynamics environment about helicopter rotors is very complex, encompassing subsonic to transonic flow with unsteady, stalled regimes and 3-D effects. Semi-empirical models of dynamic stall were created for modeling unsteady aerodynamics including stalled flow. Most of them were developed from the 1970s through the 1990s ([26], [20], [13], [27]) but failed to provide good predictions of experimental results on the case of the UH-60A in stalled regime [16]. Applied to other stalled test [28], most dynamic stall models also suffered problems of numerical convergence. Thus, there are two levels of difficulties for semi-empirical models: providing good physics description of aerodynamics and ensuring numerical convergence when implemented in comprehensive analysis codes.

The present communication is concerned about the revision of the "ONERA BH model" [27], to be named from now on "ONERA Hopf bifurcation model". This model received initially a positive review [24], but was later severely criticized for its account of shedding-vortex phenomenon in

the airfoil wake by a Van-der-Pol type equation.
The experimental results obtained in the wind tunnel S1 of Modane (France) in 1991 on the rotor 7A are considered for the illustration of the capabilities of the revised stall model. There are three flight conditions considered: the high-speed test point 312, the high-thrust test point 293 with light stall and the high-thrust test point 596 with deep stall. The computations are done with the comprehensive analysis code ROTOR of ONERA equipped with the revised dynamic stall model. Many studies have been made for the high-speed test point ([18], [1]), but no correlation studies have been published for the second experimental test point, until recently ([17], [25]). No study has been published for the third data test point.
In the next chapter, the modeling of aerodynamics is detailed, first for dynamic stall phenomenon. Aerodynamic environment for the rotor blade is inherently 3-D; so, it is necessary to introduce various effects, sweep effects, rotation effects and transonic tip relief effects. For the extreme aerodynamic condition of high-speed test point, a correction of the induced velocity, outside of the stall model, is proposed. Corrections for the test environment involving the wind tunnel walls and the test stand and for Reynolds effects are also necessary. In the third chapter, the implementation of the dynamic stall model in the comprehensive analysis code of ONERA is described. In the fourth chapter, the application of the comprehensive analysis code equipped with the dynamic stall model is made to the three different test points of the rotor 7A. Concluding remarks will be drawn in the last chapter.

2 MODELING AERODYNAMICS

Aerodynamics about the rotor results from the interaction of the incoming flow with the rotor and can be viewed as composed of a global flow that extends from far upstream of the rotor disc to far downstream, and a local flow about the rotor blades. This separation is used in comprehensive analysis to solve the aerodynamics using different methods for the global flow field and for the local flow field. Nevertheless, the two flow regions are interconnected and this feature is taken into account, the inflow conditions on the rotor blades are determined by the global flow and the aerodynamic forces acting on the blades influence the global flow. The global flow is evaluated by momentum or wake methods. The aerodynamic forces on the blades can be taken from wind tunnel experiments (generally completed by computation) and presented as tables of non-dimensional lift, drag and pitching moment coefficients with respect to aerodynamic incidence angles and Mach numbers. A number of corrections are applied to the 2-D values through models of dynamic stall. The publicized objective of dynamic stall models has been the modeling of dynamic stall aerodynamics. Actually, it involves also modeling of unsteady aerodynamics prior to the occurrence of dynamic stall. This study will be concerned with various improvements of the "ONERA Hopf Bifurcation" stall model.

2.1 Modeling Dynamic stall phenomenon

In the limited extent of this communication, it will not be possible to detail all the aspects of the dynamic stall model. Let us briefly summarize that the flow is considered as attached or still attached (due to stall delay) and separated flow. The aerodynamic coefficients $C_{1,i}$ ($i = 1,2,3$ for lift, pitching moment and drag respectively) can be separated into attached and separated components:

$$C_i = C_{1,i} + C_{2,i} \tag{1}$$

In the first regime, the aerodynamic coefficients can be separated into impulsive and circulatory components:

$$C_{1,i} = C_{1,i}^{impulsive} + C_{1,i}^{circulatory} \tag{2}$$

The values of $C_{1,i}$ vary around the static values. The latter values are obtained from the fitting of experimental polars according to analytical relations similar to those of the Leishman-Beddoes model ([2], [13], [27]).
The present dynamic stall model distinguishes from all the other models by its analysis of the separated flow. To illustrate the reasoning, consider Fig. 1 that shows the behavior of the lift coefficient during a periodic cycle of the pitching angle of an airfoil. For the state between the points 1 and 2, the flow remains attached. It is still attached up to the point 3 due to flow delay [6], although the pitching angle has increased beyond the value of the static critical angle of stall. From the point 3 to point 4, there is the stall development stage that is usually defined as uniquely the dynamic stall vortex formation. Actually, there are two flow phases ([12], [15]). In the first phase, there is formation of small scale co-rotating vortices that emerge in the shear layer, according to Mulleners et al. [15]. Then the shear layer goes through a primary instability stage, this instability is followed by a vortex formation stage, characterized by the roll-up of the shear layer into the large-scale dynamic stall DS vortex. Following its formation, the DS vortex convects towards the trailing edge of the airfoil. Between point 4 and point 7, the flow remains separated and there is formation of multiple vortices, leading to various maximum of the lift coefficient. In Fig. 1, there are only two secondary vortex, leading to two peak maximums at point 5 and 6 respectively. From point 7, the flow begins its reattachment regime.
According to the present stall model, the vortex-shedding phenomenon is simulated as a self-excited oscillator of Van-der-Pol type equation when the aerodynamic incidence angle (or angle of attack) keeps growing above the dynamic critical stall angle:

$$\frac{d^2C_{2,i}}{dt^2} - \omega_S(\beta_i^+ - \gamma_i^+ C_{2,i}^2)\frac{dC_{2,i}}{dt} + \omega_S^2 C_{2,i} = -E_i^+ \omega_S \frac{d|\alpha|}{dt} \tag{3}$$

and by a damped oscillator when the flow is reattached:

$$\frac{d^2C_{2,i}}{dt^2} - \omega_S\beta_i^- \frac{dC_{2,i}}{dt} + \omega_S^2 C_{2,i} = 0 \tag{4}$$

where $\omega_S, \beta_i^+, \gamma_i^+, E_i^+$ and β_i^- are constants. The above equations have been simplified from the original modeling [27], there is only one term proportional to $\frac{d|\alpha|}{dt}$ in the second member of Eq. 3. The Van-der-Pol equation has been used for vortex-shedding phenomenon past bluff bodies [3]. The modeling of Eq. (3-4) does not raise interest to other researchers, except a few ones [24], due to its non-linear behavior that leads to numerical difficulties for

comprehensive analysis codes.
However, according to the physical scenario described above, the excess of unsteady aerodynamic coefficient associated to the primary instability of the shear layer needs to be accounted for. Its contribution is in the same order as from the vortex formation. In the model published previously [27], this effect is not clearly stated but it is taken into account by the term $\partial C_{1,i}/\partial\alpha$ (α: aerodynamic incidence angle), obtained from the response indicial approach. Such term appears also in the ONERA-EDLIN model (first term in the right hand side of Eq. 7 of [20]). The formulation in terms of the derivatives $\partial C_{1,i}/\partial\alpha$ requires precise knowledge of the aerodynamic coefficients in the angle region around the critical stall angle that is not usually available. So, it is proposed to delete the derivative component in the first equation governing the aerodynamic coefficients and instead add the following equation:

$$\frac{d\tilde{C}_{BL}}{dt} = \lambda_{BL}(C_{BL}^{equil} - \tilde{C}_{BL}) \tag{5}$$

where:

$$C_{BL}^{equil} = \begin{cases} 0.0 & : if \quad non-stall \\ -c_{BL}^{0} \cdot \frac{df_{Bed}}{dt} \cdot \frac{c/2}{v_n} : & otherwise \end{cases} \tag{6}$$

where c_{BL}^{0} is a constant, f_{Bed} denotes the separation function introduced by Beddoes [13], v_n is the fluid velocity normal to the blade section and c is the chord.

2.2 3-D effects

The aerodynamic environment about the rotor blades is inherently 3-D. The knowledge of 3-D effects is still partial, there are ongoing studies based on experiments and CFD techniques. In comprehensive analysis, there are already semi-empirical corrections of 3-D effects. Harris [8] is the first to propose corrections for radial flow based on sweep angles. This correction leads basically to the delay of the critical stall angle. This type of correction improves the predictions, but it is not known that the variable in play is the instantaneous sweep angle or some delayed value.
In wind turbines, it is observed that the normal force is increased in inboard blade sections $r_n < 0.5$ (r_n : normalized radial distance). Such effects are called "rotation effects" and appear to be due to centrifugal and Coriolis forces [5]. Various corrections have been proposed for the aerodynamic coefficients [5], but none provides good correlation for the predictions with the experiments. In the present model, the following correction is proposed and it is limited to the normal force:

$$C_n^{rot} = \begin{cases} 0.0 : if \ \|\alpha\| \leq \|\alpha_{cr}^{3-D}\| \ and \ \|\alpha\| \leq 60.0 * (\pi/180.0) \\ c_{rot}^{0} \cdot \sin(\alpha - \alpha_{cr}^{3-D}) \cdot f_0(r_n) : \quad otherwise \end{cases} \tag{7}$$

where $f_0(r_n)$ denotes a function decaying rapidly to zero as r_n increases from 0.5:

$$f_0(r_n) = 1.0 + \tanh((0.5 - r_n)/0.10)) \tag{8}$$

There is also a new correction introduced in the stall model, associated with finite span blade effects. The phenomenon is described in Sitaraman thesis [23] as transonic tip relief effects appearing at the blade tip, leading to an important change of the pitching moment coefficient over a blade region of about 30% radius span. It is proposed to simulate the behavior of the pitching moment by the following equations:

$$C_m^{3-D} = C_m^{2-D} \cdot f_1(r_n) + C_m^{Tip} \cdot f_2(r_n) \tag{9}$$

where $f_1(r_n)$ denotes a function decaying rapidly at the blade tip and $f_2(r_n)$ decays towards inboard blade sections:

$$\left.\begin{aligned} f_1(r_n) &= \tanh((1.0 - r_n)/0.10)) \\ f_2(r_n) &= 0.50 \cdot (1.0 + \tanh((r_n - 0.82)/0.05)) \end{aligned}\right\} \tag{10}$$

The 2-D values of the pitching moment coefficient C_m^{2-D} decreases rapidly to zero near the blade tip, while the values C_m^{Tip} extends to the inboard region of the blade over a length around 0.18 r_n. The following equations govern the behavior of C_m^{Tip}:

$$\left.\begin{aligned} C_m^{Tip} &= C_m^{T1} + C_m^{T2} \\ C_m^{T1} &= (c_m^0 + c_m^1 \cdot \alpha + c_m^2 \cdot \alpha \cdot \|\alpha\| + c_m^3 \cdot \alpha^3) \cdot g(M) \cdot c_m^4 \\ C_m^{T2} &= g(M) \cdot h(\Lambda_{deg}) \cdot c_m^5 \end{aligned}\right\} \tag{11}$$

where α denotes the aerodynamic incidence angle, M the Mach number, Λ_{deg} the sweep angle in degrees, $c_m^0, c_m^1, c_m^2, c_m^3, c_m^4$ and c_m^5 are constants. The functions g and h are defined by the following relations:

$$\left.\begin{aligned} g(M) &= 0.5 + 0.25 \cdot (1.0 + \tanh((M - 0.7)/0.1)) \\ h(\Lambda_{deg}) &= 0.5 \cdot (1.0 - \tanh(\Lambda_{deg}/20.0)) \end{aligned}\right\} \tag{12}$$

According to the analytical expression for $g(M)$, the effects increase with Mach numbers but remain limited when M exceeds 0.7. The transonic tip relief effects depend also on the sweep angle, the dependence follows the law in "tanh" that limits the effects when the sweep angle exceeds 20 degrees. The variation C_m^{T1} with the aerodynamic incidence angle is suggested by the values computed by Sitaraman. The additional component C_m^{T2} that depends on sweep angles is needed to create the asymmetry, with respect to azimuth, of the values of the normal force about its minimum value at around the azimuth of 100 degrees.
The behavior of the pitching moment, described by Eq. (9-12), has been proposed, guided by physical considerations. It is possible to verify the suggested behavior by studying swept blades with high-fidelity numerical tools.

2.3 Aerodynamic correction for the high-speed flight

It is well known that comprehensive analysis fails to predict the airloads of rotors in high-speed flights. Bousman [4] raised the two main deficiencies of comprehensive analysis consisting in the predictions of the azimuthal position of the negative lift force in the advancing side of the UH-60A and the under-prediction of the pitching moment, leading to the under-prediction of the pitch link loads. These two issues have been resolved with the coupling of comprehensive analysis with CFD techniques [22]. The same issues occur for the rotor 7A and they have been recently resolved ([17], [25]). The principal difference between computation made with comprehensive analysis standalone and comprehensive analysis coupled with CFD techniques resides in the consideration of viscous effects by advanced aerodynamics methods and ignored in low-order methods.

The principal feature resulting from viscosity consideration is the phase shift in azimuthal position of the normal force for the blade sections in the tip region. To improve the capabilities of global inflow models, the following correction to the induced velocity is proposed:

$$v_{ind}^{corr} = c_{ind}^{0} \cdot \Omega \cdot R \cdot (-r_n) \cdot cos(2.0 \cdot \psi + \phi_0) \qquad (13)$$

where c_{ind}^{0} and ϕ_0 are constants, Ω denotes the rotation speed, ψ the azimuth and R the blade radius. The effects of such correction on typical values of the induced velocity at the blade tip can be visualized in Fig. 2. The maximum of the induced velocity is shifted from the azimuth at 90 degrees to higher values. Since the angle of aerodynamic incidence depends on the induced velocity, its minimum is also shifted and therefore the position of the minimum of the normal force to higher value of azimuth.

2.4 Wind tunnel effects

Since the 7A rotor is placed in the wind tunnel S1 of ONERA, the aerodynamic environment about the rotor blades is perturbed by the presence of the hub and by the wind tunnel walls. There is a correction accounting for the rotor hub and the wind tunnel wall effects made by Aerodynamics Department of ONERA in 1993 (Internal report of A. Masson and P. Beaumier), based on a surface panel method. The computation resulted into a correction of the induced velocity on the nodes positioned on the blade sections. Fig.3 shows the values of the induced velocity normalized to the incoming flow velocity (according to the direction of axis x) for the shaft angle α_q = -8.0 degrees. Only a half azimuthal region is drawn, the other half can be deduced by symmetry. It can be seen that the incoming flow is deviated by the rotor hub.
Another important effect introduced by wind tunnels concerns Reynolds numbers. Indeed, the polars (look-up tables of aerodynamic coefficients) are provided for high Reynolds numbers, in the case of the rotor 7A for the ratio R_e/M around 8 millions. The value of Reynolds numbers affects not only the critical stall angle but also the dependence of the values of the aerodynamic coefficients versus the aerodynamic incidence angles. Typically, the function f_α of the lift force versus the angle of attack is concave at high Reynolds numbers and it becomes more rounded as the Reynolds number decreases [10]. As there is no available data for the airfoils OA209 and OA213 that composed the 7A blade, the data on the family of NACA airfoils is used [10]. The correction is limited to only the values of critical stall angle and not on the shape dependence f_α. Neglecting the variation of the normal force versus the angle of attack with Reynolds number will imply the assumption of keeping the same shape dependence, this will lead to lower values of lift force at high angles of attack (greater than the critical stall angle). The experimental values of the critical stall angles for the airfoils NACA0009, NACA0012, NACA0015 and NACA2412 are reported in Fig. 4. These experimental values are fitted with the analytical expression of the following form:

$$\alpha_{cr} = c_{R_e}^{0} + c_{R_e}^{1} \cdot \tanh((R_e \cdot 1.0E^{-6} - c_{R_e}^{2})/c_{R_e}^{3}) \qquad (14)$$

where $c_{R_e}^{0}, c_{R_e}^{1}, c_{R_e}^{2}$ and $c_{R_e}^{3}$ are constants.

3 IMPLEMENTATION OF THE STALL MODEL

The Hopf bifurcation model is implemented as a module coupled to the comprehensive analysis code ROTOR of ONERA. The version of ROTOR used is a recently developed code, with predicting capabilities for the whole helicopter, instead of an isolated rotor, as in the old version developed in the 1990s. The coupling is similar to the loose coupling between comprehensive analysis code and CFD code, but with different variables for the communication between the two codes. The comprehensive analysis code sends to the stall module the values of the aerodynamic conditions on the blade nodes during a rotation period, i.e. the aerodynamic incidence angle, the pitch angle and the fluid velocity adjacent to the blade. Based on these values, the stall module will calculate the values of the airloads (normal force, pitching moment, drag and radial forces) on the blade nodes for the whole rotation period. It iterates as many times as needed to attain a periodic solution. Since the aerodynamic forces are damped rapidly, it is sufficient to run the computation for three periods. However, for the particular study of flow delay with slow time delay, it was necessary to develop a method based on Poincaré maps for calculating the periodic solution [19]. The method relies on the fact that the periodic solution of the mechanical system, if it exists, will be a fixed point for the intersection of the trajectory of the mechanical system with the phase plane at times equal to multiple integers of the period. Accordingly, the problem is reduced to the search of a fixed point by Newton's method.
The module is built for allowing the study of separate behaviors of the aerodynamic flow: quasi-steady "s", unsteady without stall "u", delayed flow "d", flow with boundary-layer effects "b" and flow with vortex-shedding phenomenon "v". It permits any combination of the various behaviors of the flow cited above. Such capabilities of the code permits separately validation of the parameters associated with each particular flow behavior. The general case with stall is determined by the option "udbv".
As stated in Eq. 2, the aerodynamic coefficients are decomposed into impulsive and circulatory components. The equations governing the unsteady behavior of the impulsive component are taken from [11]. based on thin airfoil theory. According to Johnson [11], the circulatory component is taken into account by the vortex wake model. The parameters for the delayed flow are provided by Beddoes [2]. The remaining unknown parameters are those characterizing the boundary-layer effects and the vortex-shedding phenomenon. To further simplify the model, only the equation governing the pitching moment for the behaviors of boundary layer and for vortex shedding are solved, the components of the normal and drag forces are obtained by a multiplicative constant ($4\times$ for the normal force, and $1.6\times$ for the drag force). This choice is made from the analysis of the experiments on the NACA0012 airfoil. It could be changed accordingly to the airfoil studied.
For any choice of the behavior of the aerodynamic flow, the aerodynamic forces on the blade sections of the rotor are governed by a system of ordinary differential equations ODE. With the system of ODE involving the stall phenomena (Eq. 3-4), the flow equations will contain two different regimes,

the first involving the unsteady flow without separation that varies slowly upon time while the regime involving the vortex-shedding phenomena has a rapid time-varying behavior. The system of ODE with two different behaviors with respect to time are qualified as "stiff". There are two types of ODE solvers,"non-stiff" and "stiff". The procedure for solving the system of ODE of the Hopf bifurcation model would be the use of "non-stiff" solver before stall onset and "stiff" solver at stall onset. Fortunately, there exists a solver specially developed for such circumstances, "LSODA" by Hindmarsh and Petzold in the 1980s ([9], [21]), switching automatically from non-stiff to stiff solver whenever it is needed. The use of a unique solver "stiff" or "non-stiff" is not time-efficient and may lead to numerical divergence.

The system of equations governing the mechanical behavior of the helicopter is non-linear with the addition of the equations governing the aerodynamic forces on the rotors (principal and tail). The search for an equilibrium solution is not an easy numerical task. The comprehensive analysis code ROTOR uses the solver hybrd of the package MINPACK [14]. It is based on a modification of Powell's hybrid algorithm. Although developed in the 1980s, it is quite robust and has solving capabilities comparable with other solvers. Its principal weakness consists in the request of the initial solution not too-far from the final solution; otherwise, it may diverge or take many iterations to converge.

4 APPLICATION TO THE ROTOR 7A

In 1991, ONERA made a series of experiments in the wind tunnel S1 at Modane on the rotor 7A to provide test cases for analysis. This rotor is articulated and composed of four blades with rectangular planform and a radius of 2.1 meters. The experiments were made in various configurations, from attached flow regime to stalled flow regime. This study will consider three test conditions: high-speed test point 312, high-thrust test point 293 with light stall and high-thrust test point 596 with deep stall. The last configuration was obtained by slowing the rotor speed, from its nominal speed of about 1020 rpm to about 700 rpm. Many attempts to improve analysis were made for getting a good correlation between predictions and experiments ([18], [1]) and only recently [17], the coupling of comprehensive analysis with CFD techniques meet success for the test points 312 and 293. The deep stall test point 596 is not yet considered for coupled analysis.

The computation is made for all the test points with the global flow simulated by the prescribed wake model, uniform inflow or dynamic inflow models are not used since they do not provide good values of angle of attack in the tip region of the blade.

4.1 High-speed test point 312

The high-speed test point 312, characterized by the advance ratio $\mu = 0.4$ and the lift force $\overline{Z} = 12.0$ was the case of choice for testing the capabilities of analysis in France and Germany. The comprehensive analysis code showed the same deficiencies in predictions, as for the UH-60A rotor [4], i.e. the shift in azimuthal position of the minimum of the normal force in the advancing side, and the absence of positive values of the pitching moment in the first azimuthal quadrant for the blade sections in the tip region. These two deficiencies are shown in Fig. 5 depicting the normal force and Fig. 6 depicting the pitching moment at various blade sections, for the analysis made under the assumption of quasi-steady aerodynamics. The correction due to the wind tunnel effects is not sufficient to improve the predictions: there is mainly a bump created for the normal force at the azimuth around 80^o for the blade sections of $97\%R$ and $91\%R$.

The remedy to the second deficiency of the prediction is to take account of the transonic tip relief effects on the pitching moment. As explained above, the solution has been to describe the pitching moment according to Eq.(9-12). The values of the parameters chosen for the point 312 are the following:

$$\left.\begin{array}{l} c_m^0 = -0\cdot 08, c_m^1 = 1\cdot 081E-2, c_m^2 = -1\cdot 213E-4 \\ c_m^3 = 2\cdot 855E-5, c_m^4 = 0\cdot 12, c_m^5 = 0\cdot 09 \end{array}\right\} \quad (15)$$

To create the shift of the azimuthal position of the minimum of the normal force, the correction of the induced velocity according to Eq.(13) is used with the following values of the parameters:

$$c_{ind}^0 = 0\cdot 02, \phi_0 = 38.0 \times (\pi/180.) \quad (16)$$

The correction of the induced velocity assumed according to Eq.13 is not large, as seen in Fig. 7, its main effect is to shift the position of the maximum (according to the axis convention of ROTOR) of the induced velocity at around the azimuth of 90^o to a higher value. With the conjunction of wind tunnel corrections, tip effects, rotation effects, unsteady behavior and delayed flow, the predictions of the normal force and the pitching moment are improved. They are not as good as from coupled analysis of comprehensive analysis and CFD techniques but still present much improvement compared to the initial predictions under quasi-steady aerodynamics and at the small expense of about 15 minutes of CPU time on a PC, that expense is very small compared to coupled analysis. A remark to make is about the very negative values of the pitching moment at inboard blade sections, they are due to the small number of pressure sensors on the blade (as shown in [17]). The improvement brought by to the stall model can be also visualized on the vibratory loads (harmonics 3-8 of the normal force), the stall model provides a better phase to the predictions for all the outboard sections up to the section $50\%R$ where the predictions are degraded (see Fig. 8).

The improvements of airloads lead to improved predictions of the structural loads of flap bending moment and torsion moment. For the latter, the stall model provides the phase shift, although not perfect. The amplitude predicted of the torsion moment is about 20% higher that experimental results. For the chord bending moment, the predictions are not only higher than experimental results but also contain four peaks instead of three as in experiments. It appears that the code ROTOR needs revision for the evaluation of the chord bending moment.

The rotation effects are assumed to provide improved predictions of the normal force at inboard blade section, near the rotor hub. Unfortunately, measurements on the rotor 7A were limited to inboard section at the radius of $0.50\%R$. Nonetheless, it is possible to estimate indirectly the

Table 1: High-speed flight 312: control angles and power

	θ	θ_{1c}	θ_{1s}	α_q	P (kW)
Experiments	10.41	3.43	-3.70	-13.75	88.0
QS aero.	11.28	0.99	-1.33	-13.48	98.17
W. Tun. Cor.	12.11	2.16	-1.65	-13.59	92.32
Stall model	12.11	1.20	-1.82	-13.92	95.10

Table 2: High-thrust flight 293: control angles and power

	θ	θ_{1c}	θ_{1s}	α_q	P (kW)
Experiments	8.40	3.16	-3.51	-6.70	74.80
w/o St. Mod.	10.16	1.90	-1.98	-7.90	78.13
w Stall model	7.74	1.09	-2.20	-7.37	99.92

corrections due to rotation effects. Indeed, to get the trim on the global lift of the rotor, the normal forces have to be equilibrated on all the blade sections. Since rotation effects provide more amplitude for the normal forces at inboard sections, the normal forces at outboard sections are submitted to a decrease in order to maintain the equilibrium; particularly at the section $97\%R$, the normal force at the azimuth of around 100^o decreases to attain more negative values.

The rotor control angles are the three components of the pitch angle - collective θ, longitudinal cyclic θ_{1s} and lateral cyclic θ_{1c} angles - and the shaft angle α_q. Calculations have been made under trim objectives of the experimental values of the rotor lift force $\overline{Z}$, the rotor propulsive force and Modane flapping laws (zero lateral flapping and longitudinal cyclic equal to minus longitudinal flapping angle). Table 1 lists the values of the rotor control angles from experiments, and from calculations made with quasi-steady aerodynamics, or with wind tunnel corrections or with the stall model. The values of the shaft angle calculated with all the options are reasonably correct. The values of the longitudinal cyclic calculated are different from the experiments, the difference is between 1.0^o and 2.0^o, according to the option of aerodynamics. The worst results are obtained for the lateral cyclic, with about 2.2^o of difference for the option of stall model. The predictions of power P are overestimated of about 8% from the test values. The old version of ROTOR predicts control angles that are not far from experiments, it is necessary to improve the new version for control angles calculation.

4.2 High-thrust test point 293

This test point is characterized by the advance ratio $\mu = 0.3$ and the lift force $\overline{Z} = 19.0$ The predictions of this test flight have been recently improved by coupled analysis of comprehensive analysis with CFD techniques, by teams at US. Army and ONERA [17] . However, no computation based on comprehensive analysis standalone with reasonable correlation between predictions and experimental results has been published. Computation made so far fails to detect stall. The cause is due to Reynolds effects, responsible for decreasing the critical stall angle, as shown previously in Fig. 4. With the account of critical stall angles based on the family of NACA airfoils, it is possible to correct the critical stall angle for each blade section on the blade 7A.

Through this correction, the comprehensive analysis predicts, with the stall model implemented, the appearance of stall phenomenon for this test point. The parameters of the stall model for this test point are the same as for the previous test point, except:

$$\left.\begin{array}{l} c_m^4 = -0.12 \cdot (0.3/0.4),\ c_m^5 = 0.09 \cdot (0.3/0.4) \\ c_{ind}^0 = 0.02 \cdot (0.3/0.4),\ \phi_0 = 38.0 \cdot (0.3/0.4) \end{array}\right\} \quad (17)$$

The above constants are taken equal to those of the previous test point with a multiplicative factor proportional to the advance ratio.

The values of parameters related to vortex-shedding phenomenon and boundary-layer effects are chosen as:

$$\left.\begin{array}{r} \omega_S = 0.075 \cdot 2.0 \cdot \pi;\ \beta_i^+ = 0.008;\ \gamma_i^+ = 1.700 \\ E_i^+ = 0.15;\ \beta_i^- = -3.0;\ \lambda_{BL} = 0.2 \end{array}\right\} \quad (18)$$

The predicted values of the pitching moment in Fig. 11 show negative peak values for all the blade sections, except at the blade section at $97\%R$. Computation has been made also with another comprehensive analysis code, HOST, developed by Airbus Helicopters, but with no stall model. Its results do not show any stall, due to the fact explained previously. Note that the predicted stall azimuthal region is larger than in experiments. For the normal force shown in Fig.10, the minimum at around the azimuth of 270^o is captured except for the blade section at $97\%R$. There is also a singular behavior of the normal force at the azimuth of around 70^o, it has a peak at this value and the peak is very pronounced at this blade section. The amplitude is much greater if the slope of the lift force is chosen to be given by the relationship of Prandlt-Glauert (equal to $1.0/\sqrt{(1.0-M^2)}$). In the result shown in Fig. 10, its value is chosen not to follow the above relationship but to decrease as M attains 0.8. Coupled analysis with CFD techniques indicates a very unstable behavior of aerodynamics in the first azimuthal quadrant but does not provide precise explanation. The vibratory loads are shown in Fig 12, there is improvement from the stall model, but the predictions deteriorate very quickly beginning at the blade section $82\%R$.

The structural loads, measured at only two blade sections are shown in Fig. 13. The predictions of the flap bending moment are well improved by the stall model. As for the high-speed test point, the values of the chord bending moment predicted are too high, however the number of oscillations are in agreement with the experiments. For the torsion moment, the predictions give roughly the same waveform but with a phase delay. The amplitude of the torsion moment predicted by the stall model is approximately at the same level as in experiments, while the code HOST predicts a much lower amplitude. The agreement with experiments for airloads and structural loads could be considered as reasonable with a

Table 3: High-thrust flight 596: control angles and power under fixed and trimmed control settings (C.T.)

	θ	θ_{1c}	θ_{1s}	α_q	P (kW)
Experiments	13.47	5.25	-7.06	-5.40	78.30
Fixed C.T.	13.47	5.25	-7.06	-5.40	114.44
Trimmed C.T.	14.43	4.02	-4.87	-8.01	110.54

small demand of CPU time of about 30 minutes on a PC. The coupled analysis comprehensive analysis / CFD requests at least one week of computation on multiprocessors machines.
As for the high-speed test point, the control angles given by calculations, shown in Table 2, do not have a good correlation with experiments. The value of the collective pitch angle calculated by HOST is higher than experiments of about 1.8^o, it is understandable because the aerodynamic model in this code does not provide enough lift force. The ROTOR code provides reasonable values for the shaft angle and the collective pitch angle, but as for the previous test, it gives low value of longitudinal cyclic compared with experiments, and especially very low value of lateral cyclic. For the power prediction, again this code predicts a too-high value of about 32%, compared to experiments.

4.3 High-thrust test point 596

This test point is characterized by the advance ratio $\mu = 0.3$ and the lift force $\overline{Z} = 29.2$ This flight test point has been obtained by slowing the rotor speed from its nominal speed of 1020 rpm to about 700 rpm. For this test point, unfortunately the airloads are only obtained from measurements for two blade sections, 82%R and 50%R. However, measured structural loads are obtained at four or more than four blade sections, while for the previous test points there are only measurements at two blade sections.
The computation is carried out under fixed control settings and trimmed control settings. The parameters for the stall model are chosen exactly the same as for the previous test point. Usually, the comprehensive analysis code does not succeed to obtain numerical convergence at such high values of the lift force and calculation is made under fixed control settings, given by experimental values. For both calculation options, the comprehensive analysis code ROTOR equipped with the Hopf bifurcation model succeeds to provide converged numerical solution. For airloads, the calculations provide a good correlation with experiments (Fig. 14). The number of secondary vortex shed over the blade is not correctly predicted for the blade section 82.0%R, but the amplitude of the pitching moment at stall onset is reasonably predicted. The experimental results of the normal force in the fourth azimuthal quadrant are not well reproduced by the stall model, leading to the same deficiencies for the vibratory loads (Fig.14).
The calculations under trimmed conditions provide better predictions for the flap bending moment (Fig. 15) but deviate much from experiments for the outboard sections 55%R and 75%R. They have similar waveform as in experiments, but have less oscillations. For the inboard sections at 30%R and 40%R, the correlation is good except in the range of azimuth $[0.^o,60.^o]$. For this test with great influence of dynamic stall, the amplitude of the chord bending moment predicted (Fig. 16) does not exceed too much the experimental values. The number of oscillations is visibly the same as in experiments. The predicted values of the torsion moment follow the waveform of the experimental results (Fig. 17). However, the number of oscillations is greater than observed experimentally. This feature will need more analysis.
The power prediction is very large compared to experiments, of about 40% of overestimation. One probable cause is the dependence of the lift coefficient versus the aerodynamic incidence angle, it has a shape more rounded when the Reynolds number decreases. As consequences, the lift force should get higher values for the same high value of incidence angle at low Reynolds number than at high Reynolds number. The trim objective of lift force will then be obtained at lower pitch angle, this equilibrium will lead to lower drag values and therefore lower power.

The importance of stall phenomenon can be seized through the examination of airloads and structural loads of the three test points. As the 7A rotor enters deeper in the stall regime, the pitching moment is observed to rise rapidly with an increasing amplitude at the beginning of the fourth azimuthal quadrant. This variation is the key component influencing the structural loads, particularly the torsion moment behavior that follows more closely the pitching moment (see Fig. 9, 13 and 17). The flap and chordwise bending moments acquire a richer harmonic component (see Fig. 9, 13, 15 and 16).

5 SUMMARY AND CONCLUSIONS

To attain reasonable agreement of the predictions of the comprehensive analysis with experiments on the rotor 7A, various issues have been solved at two different levels, physics modeling of aerodynamics and code implementation for ensuring numerical convergence:

1. Action of modeling aerodynamics is made at the level of global flow, outside of the stall model, for the account of the extreme aerodynamic condition of the high-speed flight. The proposed correction could be checked independently by CFD methods.

2. The Hopf bifurcation stall model has been revised to emphasize the effects of boundary-layer accompanying the formation of the dynamic stall vortex. This phenomenon is responsible for about half of the variation of the pitching moment at stall onset. This stall model is the only one to treat vortex-shedding phenomenon as a non-linear effect governed by ordinary differential equations.

3. Comprehensive analysis use look-up tables for values of aerodynamic coefficients and thus are time-efficient means for predictions of the aeromechanical behavior of the rotor. These tables provide 2-D values of aerodynamic coefficients. Various corrections are necessary for taking into account the 3-D effects, they are based on sweep effects, rotation effects and transonic tip relief effects.

4. The procedure for the implementation of the Hopf bifurcation model to the comprehensive analysis code ROTOR of ONERA has been presented. The numerical code established is robust and allows convergence in the deep-stall

test point of the rotor 7A.

5. The application of the comprehensive analysis code ROTOR equipped with the stall model has been illustrated on three test points of the rotor 7A carried out in the wind tunnel S1 of ONERA, involving high-speed and high-thrust test points. For all test points, the predictions of airloads are in reasonable agreement with experiments and request about 35 minutes on a PC for the stalled test point and less for the high-speed test point. Improvement of airloads predictions leads to improved predictions of structural loads.

6. ACKNOWLEDGMENTS

The author would like to express thanks to Mr. D.Petot for his explanations about the use and the architecture of the code ROTOR.

References

[1] Beaumier P., Costes M., Rodriguez B., Poinot M., Cantaloube B., *" Weak and strong coupling between the elsA CFD solver and the HOST helicopter*," 31st European Rotorcraft Forum Proceedings, Florence, Italy September 13-15, 2005.

[2] Beddoes T.S., *"Representation of Airfoil Behavior*," Vertica 7(2), pp.183-197, 1983.

[3] Blevins R.D., *"Flow-Induced Vibration*," 2nd edn. Van Nostrand Reinhold, 1990.

[4] Bousman W. G., *"Putting the Aero Back Into Aeroelasticity*," Eighth ARO Workshop on Aeroelasticity of Rotorcraft Systems, University Park, PA, U.S.A, October 18-20, 1999.

[5] Breton S-P., Coton F.N., Moe G.,*"A Study on Rotational Effects and Different Stall Delay Models Using a Prescribed Wake Vortex Scheme and NREL Phase VI Experiment Data*," Wind Energ. 11, pp. 459 - 482, 2008.

[6] L.E. Ericsson, J.P. Reding., *"Fluid mechanics of dynamic stall Part I. Unsteady flow concepts*," Journal of Fluids and Structures 2, pp. 1-33, 1988.

[7] Guckenheimer J., Holmes P., *"Nonlinear Oscillations, Dynamical Systems, and Bifurcations of Vector Fields (Applied Mathematical Sciences)*," Springer, 1st ed. 1983. Corr. 6th printing 2002 Edition.

[8] Harris F.D., Tarzanin. F.J. , Fisher R.K., *"Rotor High Speed Performance, Theory vs Test*," AHS Journal, vol. 15, no. 3, July 1970.

[9] Hindmarsh A.C., *"A Systematized Collection of ODE Solvers*," Scientific Computing, R. S. Stepleman et al. (eds.), North-Holland, Amsterdam (vol. 1 of IMACS Transactions on Scientific Computation), pp. 55-64, 1983.

[10] Jacobs E.N., Sherman A., *"Airfoil section characteristics as affected by variations of the Reynolds number*," NACA-Report 586, 1937.

[11] Johnson, W., *"Rotorcraft Dynamics Models for a Comprehensive Analysis*," AHS 54th Annual Forum Proceedings, Washington, D.C., May 20-22, 1998.

[12] Jumper E.J., Stephen F.J., *"Toward Unsteady Lift Augmentation: An Assessment of the Role of Competing Phenomena in Dynamic Stall*," Proceedings of the Second AFOSR Workshop on Unsteady Separated Flows, Colorado, 28-29 July, 1987.

[13] Leishman J., Beddoes T., *"A semi-empirical model for dynamic stall*," Journal of the American Helicopter Society 34 , pp. 317, 1989.

[14] Moré J.J., Garbow B.S., Hillstrom K.E., *" User Guide for MINPACK-1*," Argonne National Laboratory Report ANL-80-74, Argonne, Ill., 1980.

[15] Mulleners K., Raffel M., *"Dynamic stall development*," Experiments in Fluids 54(2), pp. 1469 - 1477, 2013.

[16] Nguyen K., Johnson W., *"Evaluation of Dynamic Stall Models with UH60A Airloads Flight Test Data*," AHS 54th Annual Forum Proceedings, Washington D.C., U.S.A., May 20-22, 1998.

[17] Ortun B., Potsdam M., Yeo H. , Truong K.V., *"Rotor Loads Prediction on the ONERA 7A Rotor using Loose Fluid/Structure Coupling*," AHS 72nd Annual Forum Proceedings, West Palm Beach, Florida , U.S.A., May 17-19, 2016.

[18] Pahlke K. , van der Wall B. G., *"Chimera Simulations of Multibladed Rotors in High-Speed Forward Flight with Weak Fluid-Structure-Coupling*," 29th European Rotorcraft Forum Proceedings, Friedrichshafen,Germany, September 16-18, 2003.

[19] Parker T.S., Chua L.O.,*"Practical numerical algorithms for chaotic systems* ," Springer-Verlag New York Inc., 1989.

[20] Petot D., *"Differential Equation Modeling of Dynamic Stall*," La Recherche Aérospatiale , No. 1989:6, 1989.

[21] Petzold L.R., *"Automatic selection of methods for solving stiff and nonstiff systems of ordinary differential equations*," SIAM J. Sci. Statist. Comput., 4 , pp. 136 148, 1983.

[22] Potsdam M., Yeo H., Johnson W., *"Rotor Airloads Prediction Using Loose Aerodynamic/Structural Coupling*," Journal of Aircraft, Vol. 43(3), pp. 732 - 742, 2006.

[23] Sitaraman J., *"CFD based unsteady aerodynamic modeling for rotor aeroelastic analysis*," Department of Aerospace Engineering . PhD Thesis , University of Maryland, College Park, MD, U.S.A., 2003.

[24] Snel H., *"Review of the Present Status of Rotor Aerodynamics*," Wind Energy, vol.1, pp. 46-69, 1998.

[25] Surrey S., Ortun B., Truong K.V., Wienke F.,*"Advanced modeling of the 7A structural rotor blade dynamics*," AHS 72nd Annual Forum Proceedings, West Palm Beach, Florida, U.S.A., May 17-19, 2016.

[26] Tran C.T., Petot D., *"Semi-empirical model for the dynamic stall of airfoils in view of the application to the calculation of responses of a helicopter blade in forward flight*," Vertica, 5 (1) , pp. 3553, 1981.

[27] Truong K.V., *"A 2-D dynamic stall model based on Hopf bifurcation*," 19th European Rotorcraft Forum Proceedings, Cernobbio (Como), Italy, Sept. 14-16,1993.

[28] Yeo H., *"Calculation of Rotor Performance and Loads Under Stalled Conditions*," AHS 59th Annual Forum Proceedings, Phoenix, Arizona, U.S.A., May 6-8, 2003.

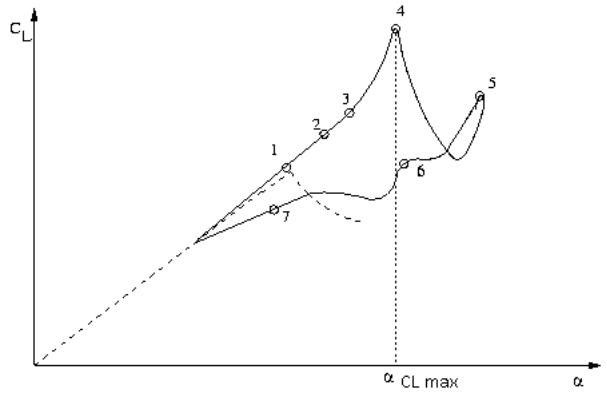

Fig. 1: Lift force of an airfoil pitching in deep stall regime

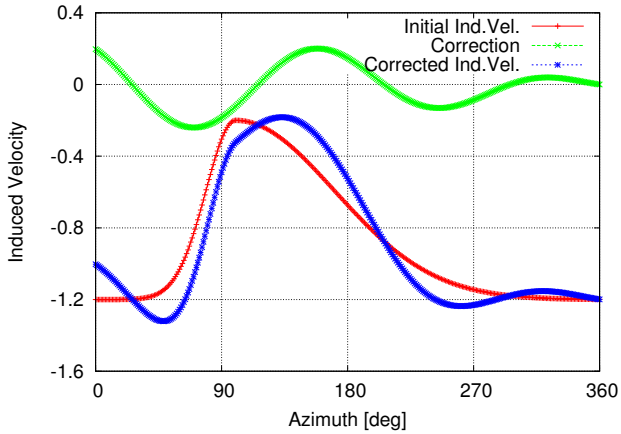

Fig. 2: Correction of Induced velocity for high-speed flights

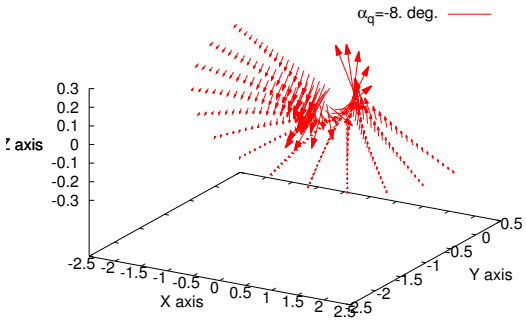

Fig. 3: Correction of Induced velocity due to the presence of the test stand and wind tunnel walls

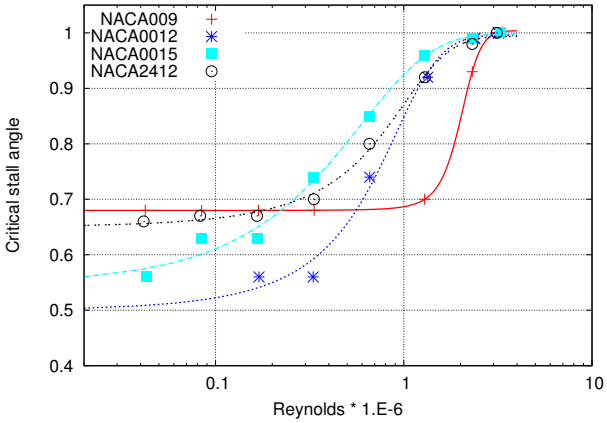

Fig. 4: Variation of the critical stall angle of various NACA airfoils with respect to Reynolds numbers

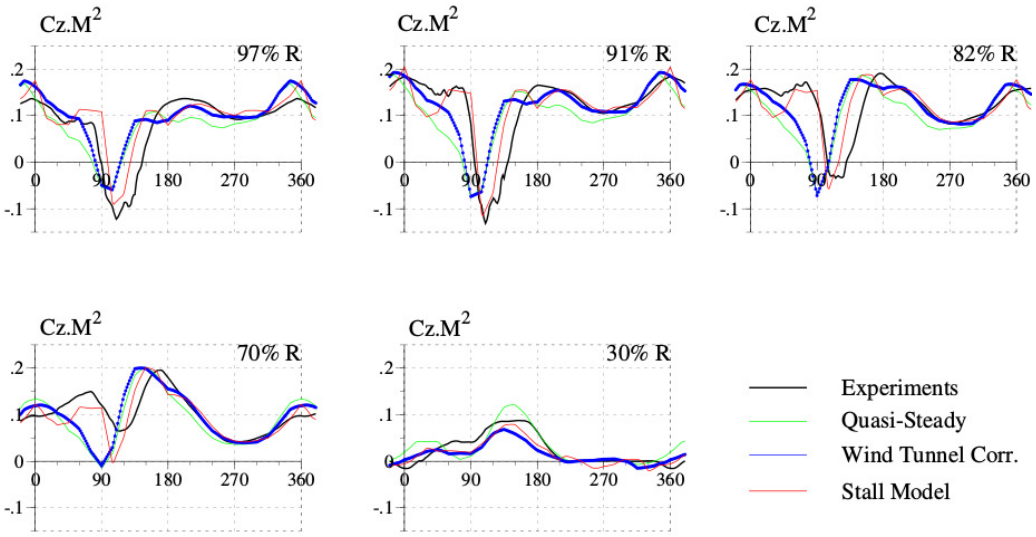

Fig. 5: Normal force for the high-speed test point of the rotor 7A

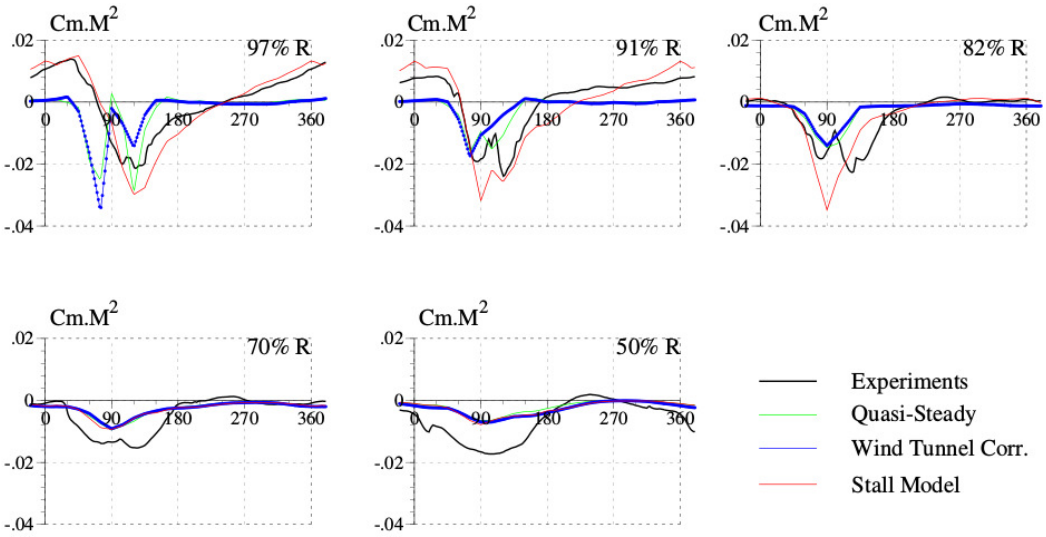

Fig. 6: Pitching moment for the high-speed test point of the rotor 7A

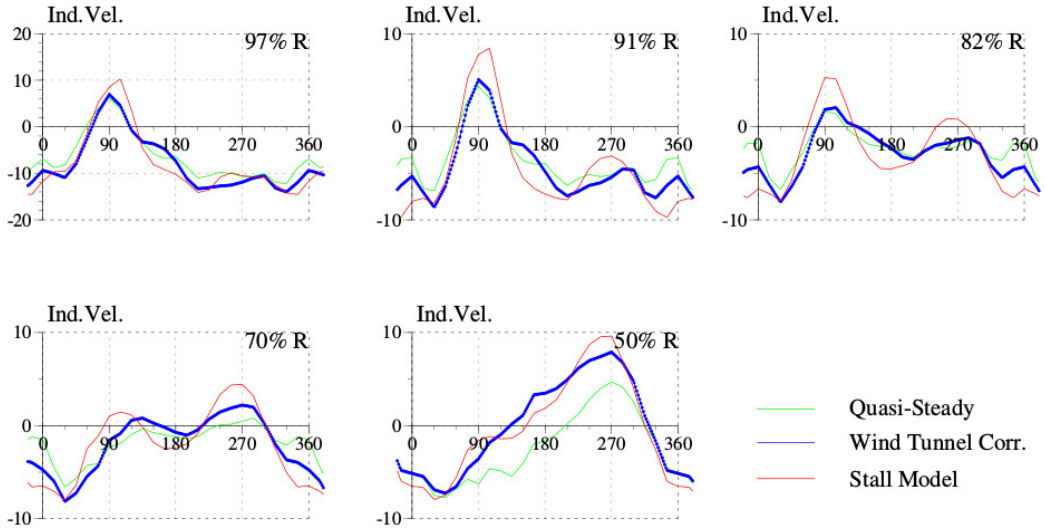

Fig. 7: Induced velocity for the high-speed test point of the rotor 7A

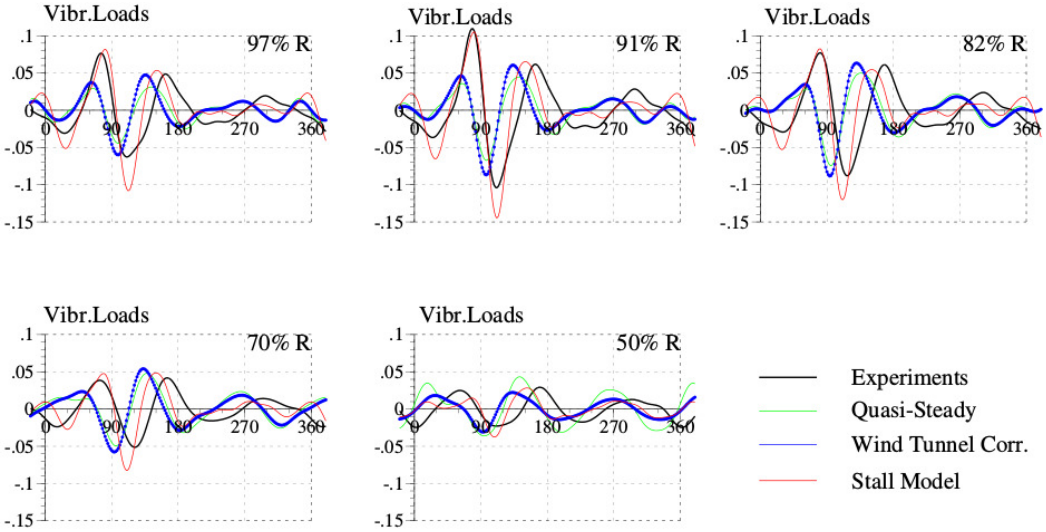

Fig. 8: Vibratory loads for the high-speed test point of the rotor 7A

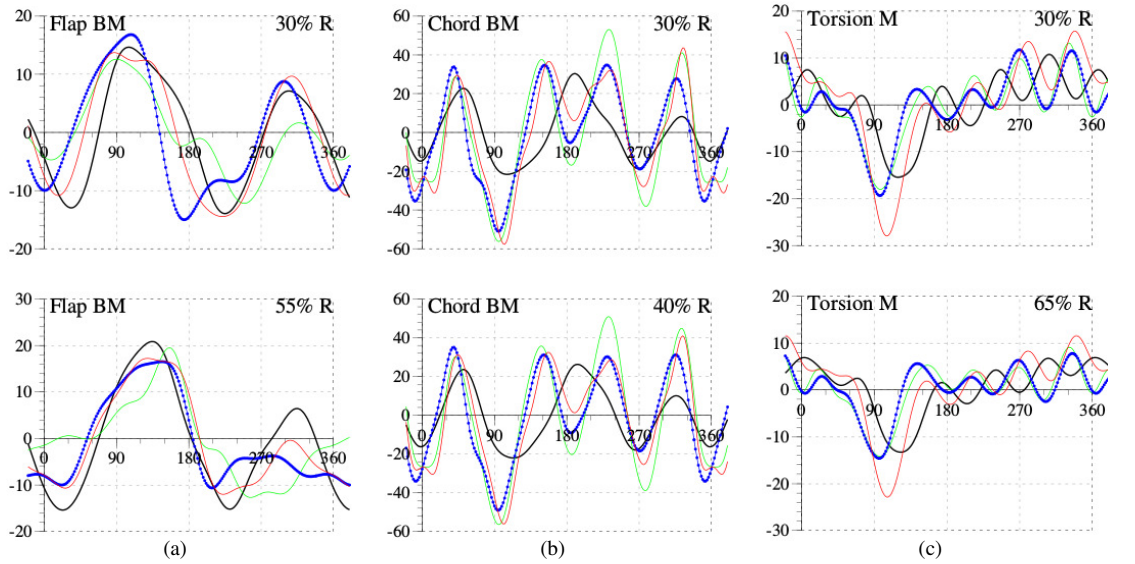

Fig. 9: Structural loads for the high-speed test point of the rotor 7A:

(a)Flap Bending Moment, (b) Chord Bending Moment, (c) Torsion Moment

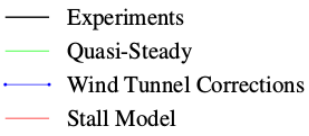

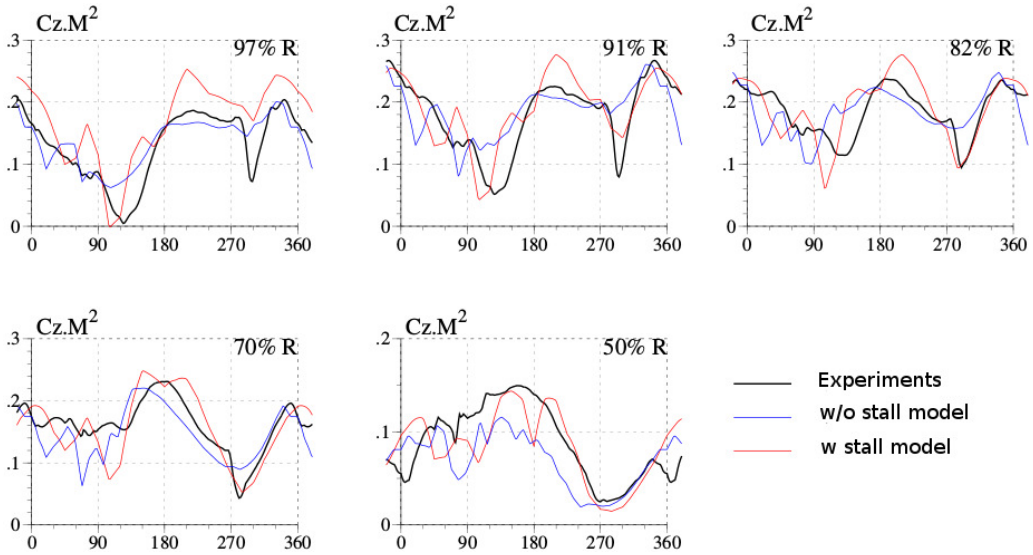

Fig. 10: Normal force for the high-thrust test point 293 of the rotor 7A

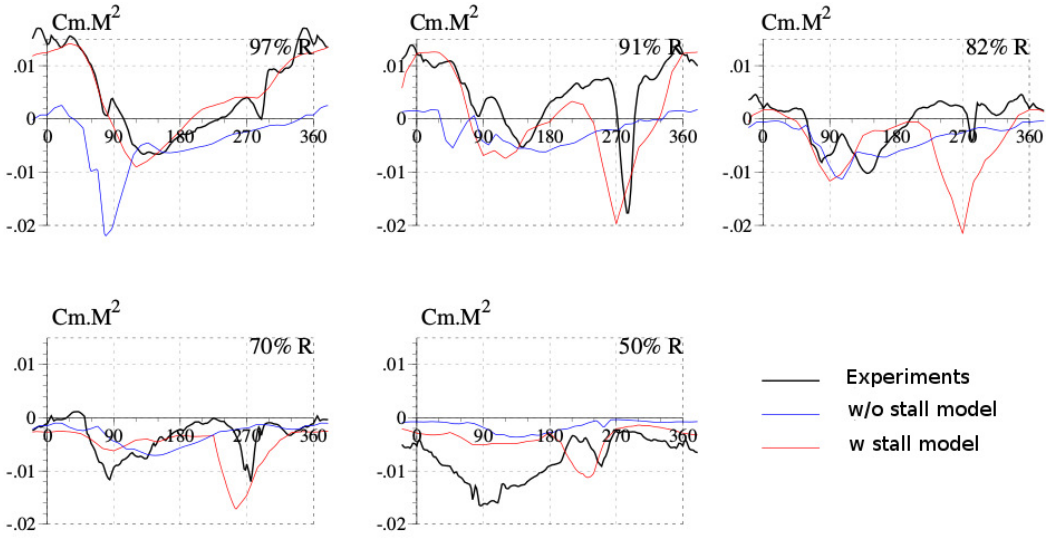

Fig. 11: Pitching moment for the high-thrust test point 293 of the rotor 7A

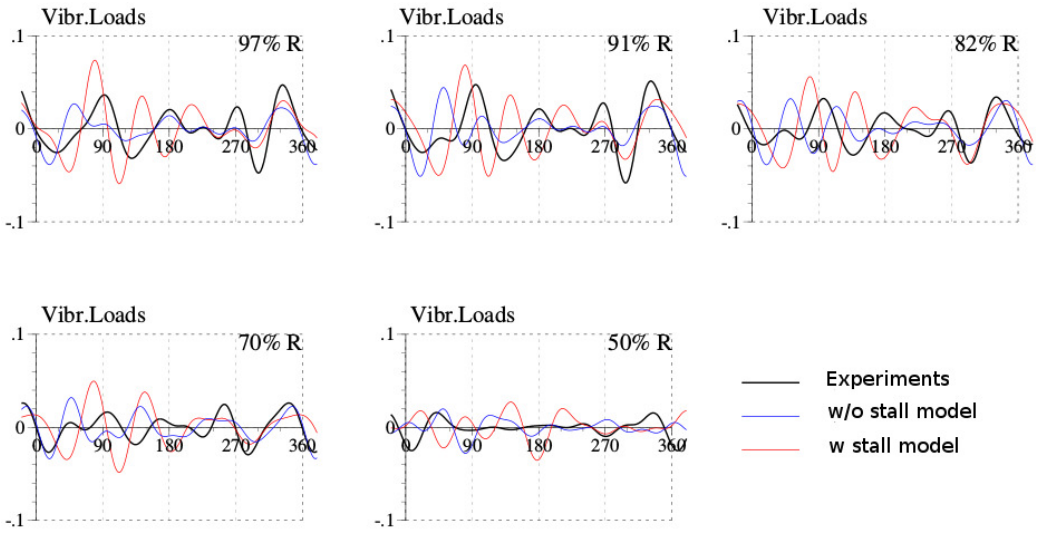

Fig. 12: Vibratory loads for the high-thrust test point 293 of the rotor 7A

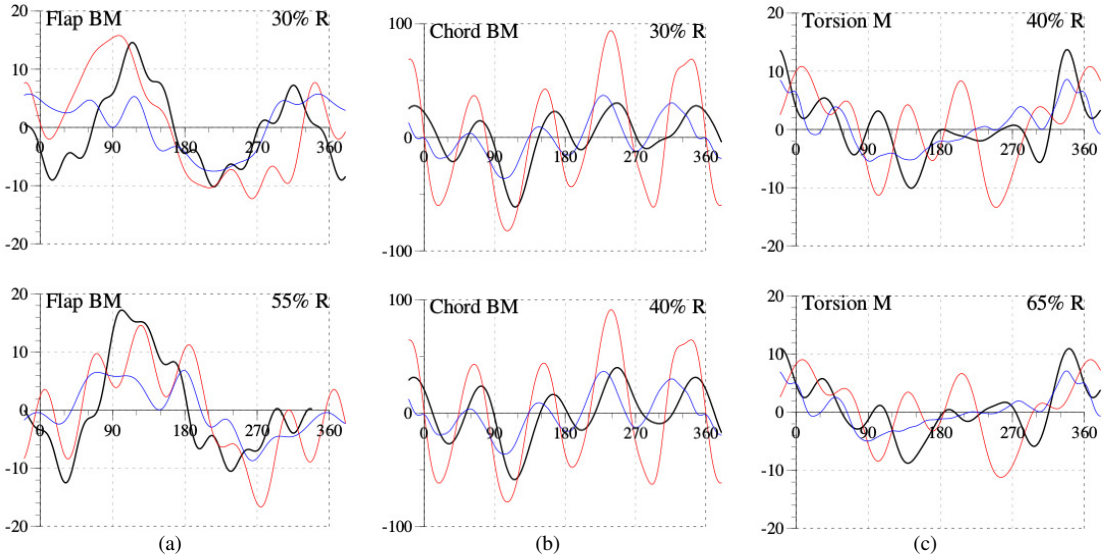

Fig. 13: Structural loads for the high-thrust test point 293 of the rotor 7A:

(a) Flap Bending Moment, (b) Chord Bending Moment, (c) Torsion Moment

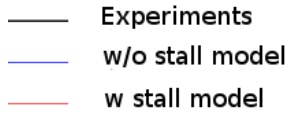

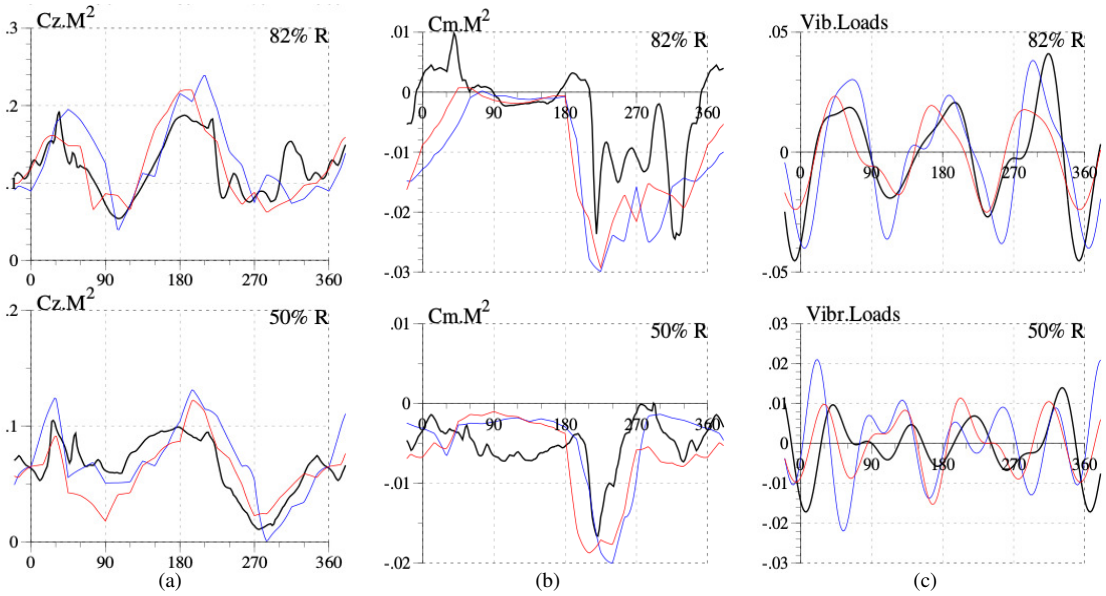

Fig. 14: Airloads for the high-thrust test point 596 of the rotor 7A:

(a) Normal force, (b) Pitching moment, (c) Vibratory loads

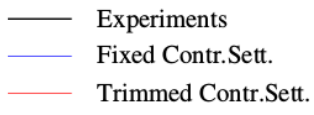

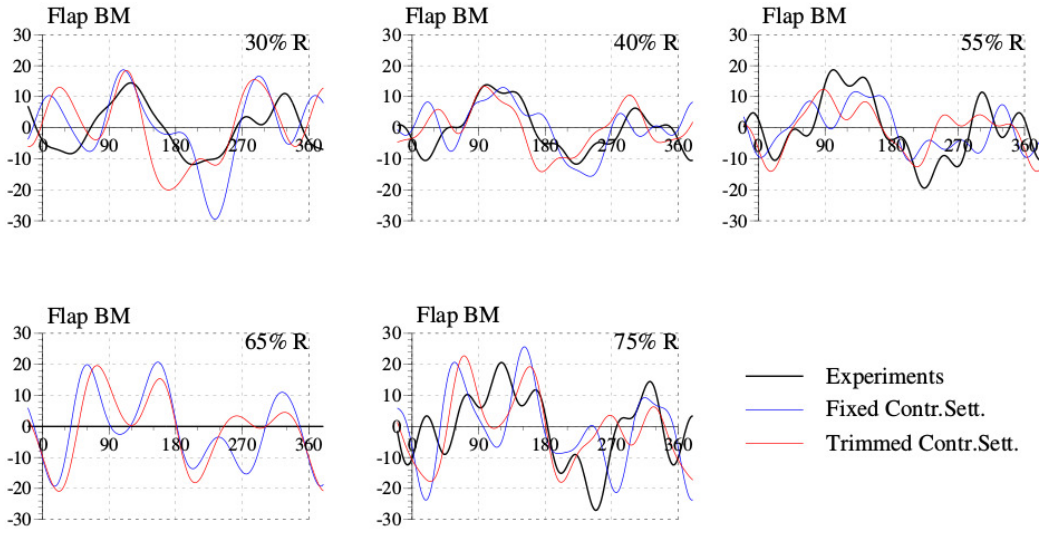

Fig. 15: Flap bending moment for the high-thrust test point 596 of the rotor 7A

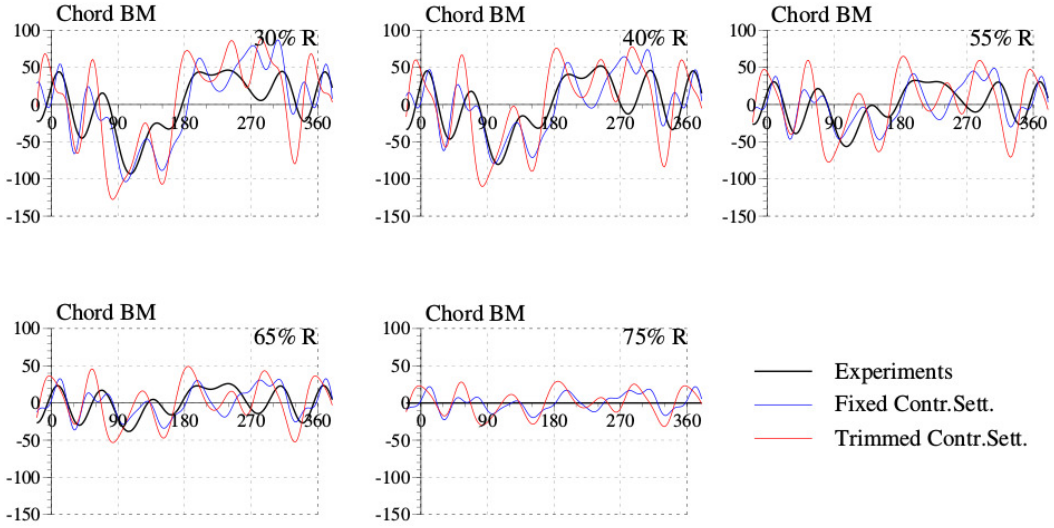

Fig. 16: Chord bending moment for the high-thrust test point 596 of the rotor 7A

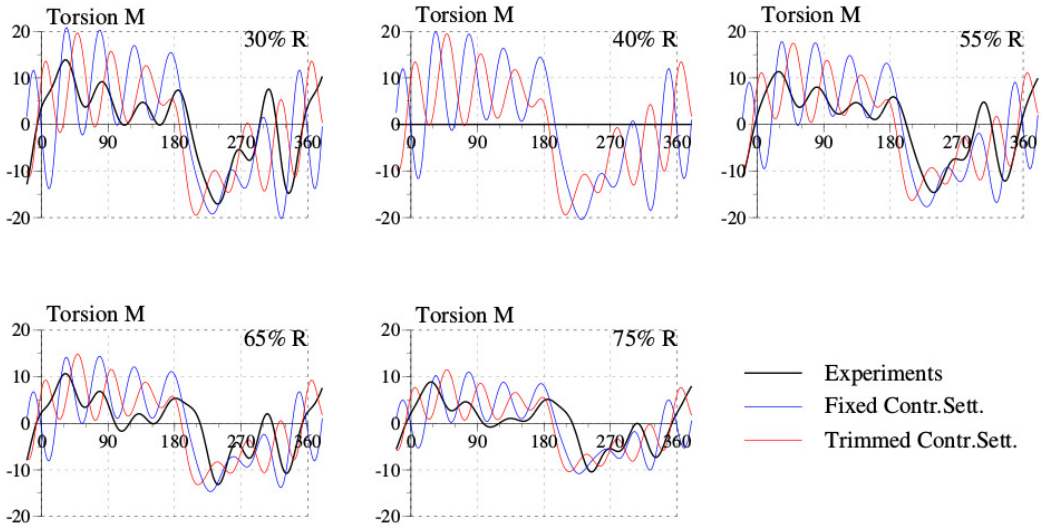

Fig. 17: Torsion moment for the high-thrust test point 596 of the rotor 7A